

# Stabilization of a Mach 6 Boundary Layer Using a Two-Dimensional Cavity

Jiaao Hao\* and Chih-Yung Wen†

*The Hong Kong Polytechnic University, Kowloon, Hong Kong*

**The stability of a hypersonic boundary layer over a flat plate to wall blowing-suction with the effect of a two-dimensional cavity at different locations is investigated using direct numerical simulations. The results indicate that the second mode is damped when the cavity is placed closely downstream of the synchronization point of mode F and mode S, whereas the effect is reversed if it is located upstream and further downstream of the synchronization point. Strong damping of the disturbances is observed inside the cavity, which is found to be consistent with the thermoacoustic interpretation. It is suggested that an efficient way to stabilize the boundary layer dominated by the second-mode instabilities is to put a local cavity in the close downstream region of the synchronization point corresponding to the most dangerous frequency.**

## I. Introduction

The performance of hypersonic vehicles is significantly affected by the boundary-layer laminar–turbulent transition, which can greatly increase the surface heating and frictional drag and lead to a considerable decrease in the payload capacity.

In a weak-disturbance environment that are frequently encountered by a hypersonic vehicle, the path to transition comprises three stages including receptivity, linear eigenmode growth, and nonlinear breakdown to turbulence [1]. Compared to subsonic and moderate-supersonic flows, the transition mechanisms of hypersonic boundary layers are much more complex and much less understood. In addition to the first mode corresponding to the compressible counterpart of Tollmien–Schlichting waves, there are the second, third, and higher modes interpreted as trapped acoustic waves [2]. For hypersonic boundary-layer flows over a flat plate, mode F originates from the fast acoustic wave, whereas mode S (or the first mode) originates from the slow acoustic wave near the leading edge through the receptivity process. The phase velocities of mode F and mode S intercept at the so-called synchronization point, where the two modes exchange energy and excite the second mode (either mode F or mode S). Under high Mach number conditions, the second-mode instabilities can dominate the transition process.

To control the second-mode instabilities, multiple techniques have been proposed including local heating or cooling trips [3], roughness elements [4,5], and porous coatings [6]. In these studies, the relative positions of these elements to the synchronization point of mode F and mode S have been found to be critical to the control effectiveness. For example, it was found that the second mode is amplified when a heating trip is located upstream of the synchronization point, whereas the effect is reversed if it is placed downstream [3]. Similar trend has also been demonstrated for local roughness elements and porous coatings.

Recently, Bountin et al. [7] found that the second mode could be strongly suppressed using a wavy surface composed of multiple small cavities by means of direct numerical simulations (DNS) and experiments. A series of shallow cavities that generate relatively stable shear layers was used to stabilize the second-mode waves, while avoiding exciting any detrimental acoustic resonances. This idea was inspired by the numerical study addressing the stability of hypersonic boundary layers over a compression corner [8]. It was shown that the second mode grows exponentially in the regions upstream of the separation bubble and downstream of the reattachment shock wave, whereas it remains neutral in the separation region. It is important to note that the flow structure in the vicinity of the separation bubble is similar to that behind a local roughness element. Therefore, the cavity location relative to the synchronization point of mode F and mode S is also supposed to be critical to the wavy-wall stabilization concept.

---

\*Research Assistant, Department of Mechanical Engineering, [jiaao.hao@polyu.edu.hk](mailto:jiaao.hao@polyu.edu.hk).

†Professor, Department of Mechanical Engineering, [cywen@polyu.edu.hk](mailto:cywen@polyu.edu.hk).

The objective of this study is therefore to investigate the effect of cavity location on the stabilization of a hypersonic boundary layer using DNS. Simulations of a Mach 6 flat-plate boundary layer with a local two-dimensional cavity placed at different locations are performed to identify the role of the synchronization point.

## II. Governing Equations

The governing equations are the two-dimensional compressible Navier–Stokes equations in the following conservative form:

$$\frac{\partial \mathbf{U}}{\partial t} + \frac{\partial (\mathbf{F} - \mathbf{F}_v)}{\partial x} + \frac{\partial (\mathbf{G} - \mathbf{G}_v)}{\partial y} = 0. \quad (1)$$

Here, the vectors of the conservative variables and the vectors of the inviscid and viscous fluxes in the  $x$  direction are, respectively, given by

$$\mathbf{U} = \begin{pmatrix} \rho \\ \rho u \\ \rho v \\ \rho e \end{pmatrix}, \quad \mathbf{F} = \begin{pmatrix} \rho u \\ \rho u^2 + p \\ \rho uv \\ (\rho e + p)u \end{pmatrix}, \quad \mathbf{F}_v = \begin{pmatrix} 0 \\ \tau_{xx} \\ \tau_{xy} \\ u\tau_{xx} + v\tau_{xy} - q_x \end{pmatrix}, \quad (2)$$

where  $\rho$  is the density,  $u$  and  $v$  are the velocities in the  $x$  and  $y$  directions, respectively,  $p$  is the pressure, and  $e$  is the specific total energy. The flux vectors in the  $y$  direction have similar expressions.

The fluid is assumed to be a perfect gas with the specific heat ratio  $\gamma = 1.4$ . The viscous stresses are modeled assuming a Newtonian fluid and Stokes' hypothesis, and the heat fluxes are calculated using Fourier's law. The dynamic viscosity is evaluated using Sutherland's law, and the coefficient of conductivity is determined via a constant Prandtl number  $Pr = 0.72$ .

## III. Computational Details

### A. Geometry and flow conditions

The flat plate has a length of 0.2 m. The schematic of the local cavity is illustrated in Fig. 1. The length of the cavity is  $l = 12$  mm, and the depth is  $d = 1.8$  mm corresponding to the boundary-layer thickness. The length-to-depth ratio is  $l/d = 6.67$  so that it can be regarded as a shallow cavity. The dimensions are chosen to be the same as those used in Bountin et al. [7].

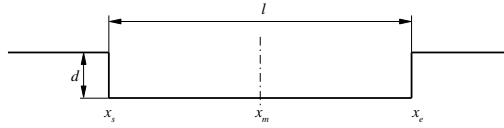


**Fig. 1 Schematic of the cavity geometry.**

The freestream conditions are specified as follows: the Mach number  $M_\infty = 6.0$ , the unit Reynolds number  $Re_\infty = 10.5 \times 10^6 \text{ m}^{-1}$ , and the static temperature  $T_\infty = 43.18$  K. The wall is assumed to be isothermal with  $T_w = 293$  K. Note that the flow density, velocities, pressure, and temperature are nondimensionalized by  $\rho_\infty$ ,  $u_\infty$ ,  $\rho_\infty u_\infty^2$ , and  $T_\infty$ , respectively.

### B. Flow solver

The numerical simulations are performed using a multiblock parallel finite-volume CFD code called PHAROS [9]. It has been successfully applied to hypersonic thermochemical nonequilibrium simulations over capsule, double-cone, and hollow-cylinder/flare configurations [10–13]. In this study, PHAROS is extended to higher order for hypersonic transition simulations. The inviscid terms are calculated using the modified Steger–Warming scheme [14]. The ninth-order upwind scheme is used for the reconstruction of dependent variables in smooth regions, whereas the second-order MUSCL reconstruction [15] with the van Leer slope limiter is used near discontinuities. The viscous fluxes are calculated using the second-order central difference scheme.

### C. Simulation strategy

The computational mesh is constructed with 1500 and 200 nodes in the  $x$  and  $y$  directions, respectively. There are approximately 100 grids within the boundary layer. For the cavity cases, approximately  $100 \times 100$  nodes are distributed in the domain of the separated flow. Grid independence was verified using a finer grid with  $3000 \times 400$  nodes in the main domain and  $200 \times 200$  nodes inside the cavity.

The simulation strategy contains two steps. First, the steady base flow is computed with a large Courant–Friedrichs–Lewy (CFL) number of 1000 to achieve fast convergence using a line relaxation method [16]. In the second step, after disturbances are introduced using a local blowing-suction actuator on the wall, time-accurate unsteady simulations are performed using an explicit third-order Runge–Kutta method. The induced mass flux by the actuator is determined by

$$\frac{\rho_w v_w}{\rho_\infty u_\infty} = \varepsilon \sin\left(2\pi \frac{x-x_1}{x_2-x_1}\right) \sin(2\pi f), \quad (3)$$

where  $x_1 = 10$  mm,  $x_2 = 15$  mm, and  $f = 138.74$  kHz. The forcing amplitude is set to  $\varepsilon = 10^{-3}$  to ensure the linear evolution of the excited disturbances.

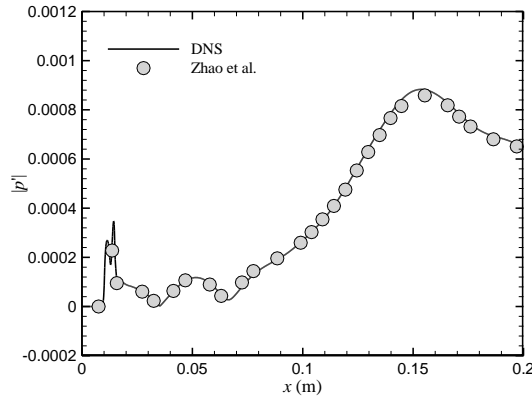
### D. Validation

To evaluate the accuracy of the present simulations, the results for the baseline flat-plate case are compared with the DNS data of Zhao et al. [1] and the predictions from the linear stability theory (LST). The instantaneous pressure perturbation is processed using the Fourier transformation to obtain the pressure perturbation amplitude  $|p'|$  and phase angle  $\varphi'$ . In a spatial stability problem, the local wave number can be defined via

$$\alpha_r = \sqrt{\frac{\mu_\infty x}{\rho_\infty u_\infty}} \frac{d\varphi'}{dx}, \quad (4)$$

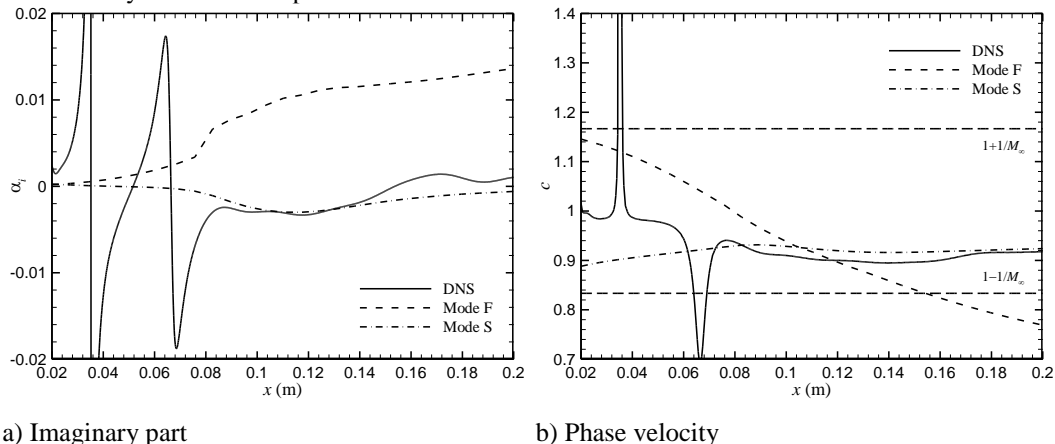
$$\alpha_i = -\sqrt{\frac{\mu_\infty x}{\rho_\infty u_\infty}} \frac{1}{|p'|} \frac{d|p'|}{dx}. \quad (5)$$

Figure 2 compares the calculated evolution of pressure perturbation amplitude along the surface with that predicted by Zhao et al. [1]. In Ref. [1], DNS were performed using a fifth-order upwind compact scheme and a sixth-order central difference scheme to discretize the inviscid and viscous fluxes, respectively. As seen from the figure, good agreement is obtained. There are strong modulations of pressure perturbation amplitude downstream of the actuator, which can be attributed to the coexistence of mode F, mode S, acoustic waves, and entropy and vorticity waves [17]. After  $x \approx 0.1$  m, mode S has become the dominant mode leading to an exponential increase in the pressure perturbation amplitude.



**Fig. 2 Comparison of the pressure perturbation amplitude obtained from DNS and that predicted by Zhao et al. [1].**

Figure 3 compares the imaginary part of the wave number and the phase velocity obtained from numerical simulations and those of mode F and mode S from LST. According to the LST predictions, mode F is always stable, whereas mode S is unstable from  $x = 0.044$  m. The synchronization point of mode F and mode S corresponding to  $f = 138.74$  kHz is located at  $x = 0.105$  m. Strong oscillations of growth rate and phase velocity before the synchronization point are also caused by the coexistence of different modes. According to Fedorov et al. [18], mode S evolves from the first mode to the second mode in the vicinity of the synchronization point and becomes dominant further downstream. Consequently, the growth rate and phase velocity obtained from DNS agree well with those of mode S from LST after the synchronization point.



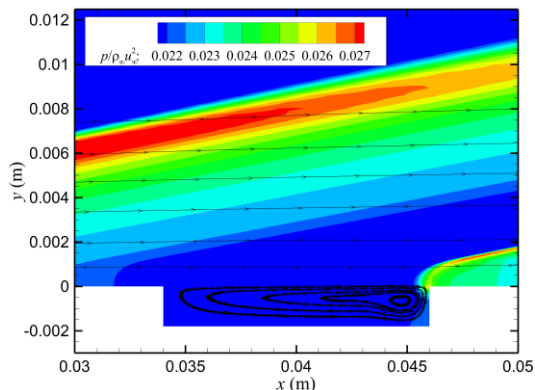
**Fig. 3 Comparison of the wave number obtained from DNS and those of mode F and mode S from LST.**

#### IV. Results

In this study, four cases with different cavity locations are considered with  $x_m = 0.04, 0.08, 0.12,$  and  $0.16$  m, respectively. For the wall blowing-suction actuator with  $f = 138.74$  kHz, the cavity is located upstream of the synchronization point of mode F and mode S for cases 1 and 2, whereas it is placed downstream of the synchronization point for cases 3 and 4.

##### A. Steady solution

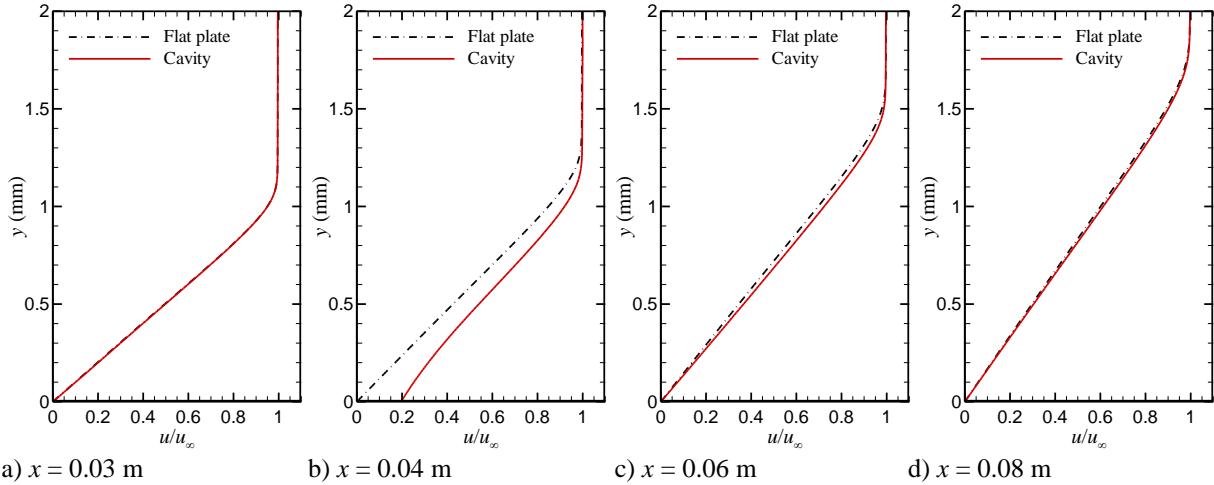
The simulated steady base flow around the cavity for case 1 is shown in Fig. 4. There is a weak shock wave generated near the flat-plate leading edge due to the viscous interaction as seen from the pressure contour. From the streamline pattern, the flow separates from the leading edge of the cavity resulting in a shear layer bridging the length of the cavity. A compression wave can be observed near the cavity trailing edge induced by the shear layer impingement. It is important to note that no self-sustaining oscillations occur in the base flow.



**Fig. 4 Pressure contour and streamline pattern around the cavity for case 1.**

Figure 5 shows the streamwise velocity profiles in the wall-normal direction at different locations for case 1. The baseline flat-plate results are also plotted. Clearly, the flow is almost unaffected in the upstream region of the cavity. At  $x = 0.04$  m located at the middle of the cavity, the velocity profile is strongly distorted presenting a thinner boundary layer and a nonzero velocity at  $y = 0$  m. Downstream of the cavity, deviation from the baseline results decreases and

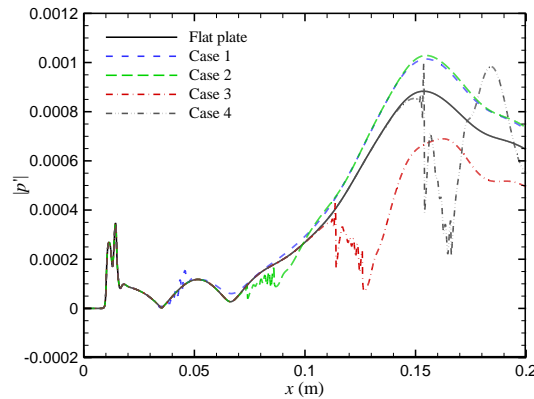
the velocity profile without cavity is eventually reestablished after  $x = 0.08$  m. The results indicate that the cavity only has local effects on the steady base flow similar to the numerical observations on the boundary-layer flow around a local roughness element [5].



**Fig. 5 Distributions of streamwise velocity in the wall-normal direction at different locations for case 1.**

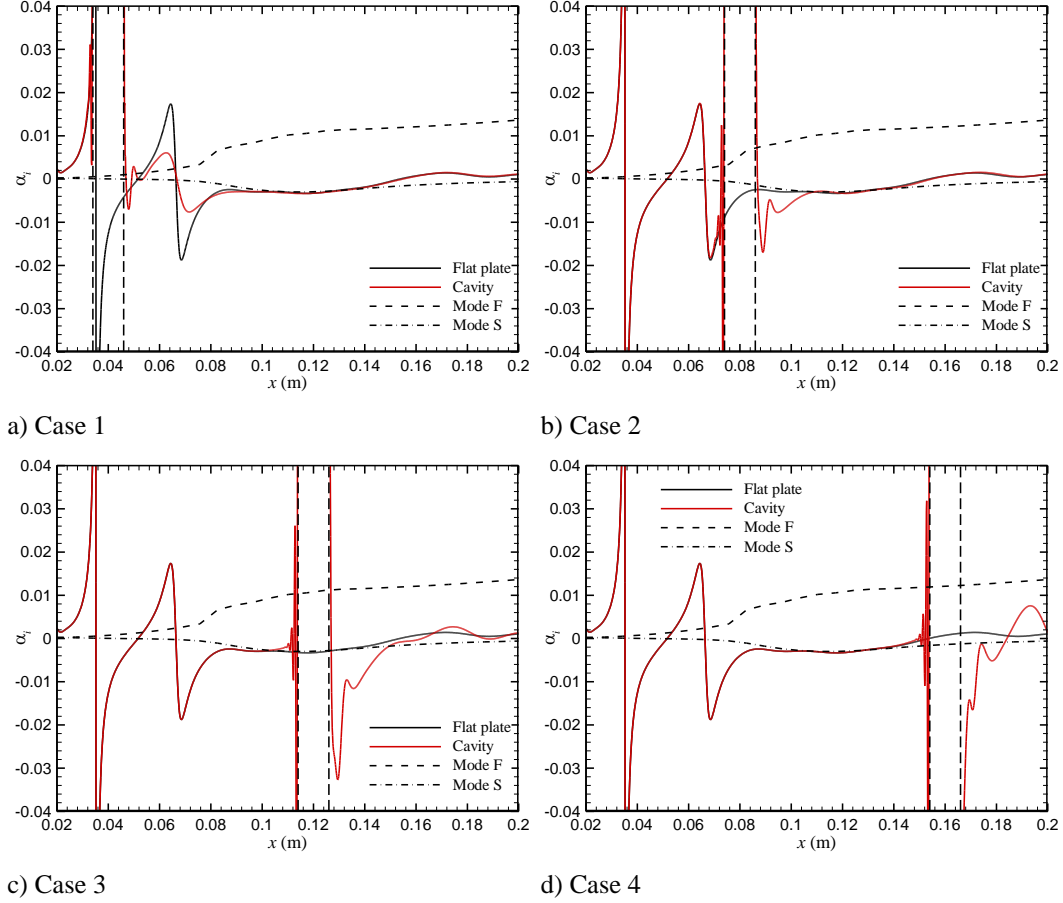
### B. Effect of cavity location on boundary-layer stability

Figure 6 compares the pressure perturbation amplitudes along the surface for different cases with the baseline flat-plate result. For the baseline case, the second mode starts to amplify exponentially after the synchronization point and reaches its maximum at  $x \approx 0.150$  m. Clearly, the development of the pressure perturbation is unaffected upstream of the cavity. When the cavity is placed upstream of the synchronization point (cases 1 and 2), the maximum amplitude is increased compared with the baseline value. In contrast, the second mode is stabilized when the cavity is located closely downstream of the synchronization point (case 3). However, as the cavity moves further downstream (case 4), the pressure perturbation is amplified again. It is interesting to note that there is no significant change in the disturbance amplitude across the cavity for cases 1 and 2, whereas the pressure perturbation amplitude is significantly reduced for cases 3 and 4. The results indicate that the unstable second mode is destabilized when the cavity is placed upstream and further downstream of the synchronization point and stabilized only when the cavity is located closely downstream of the synchronization point.



**Fig. 6 Distributions of the pressure perturbation amplitudes along the surface for different cases.**

Figure 7 compares the imaginary parts of the wave number for different cases with the baseline flat-plate result and those of mode F and mode S obtained from LST. Again, the cavity only has local effect on the development of disturbances especially for cases 1 and 2. The baseline result is recovered further downstream of the cavity and the numerical results agree well with the theoretical prediction of mode S. Note that the growth rates immediately after the cavity are much larger than that for the flat plate for cases 3 and 4, which corresponds to the steep increase in the pressure perturbation amplitude as shown in Fig. 6. For case 4, even though the disturbances are significantly reduced across the cavity, the growth rate after the cavity increases so much that the perturbation amplitude experiences a strong growth and exceeds the flat-plate result.



**Fig. 7 Distributions of the imaginary parts of the wave number along the surface for different cases. The dashed vertical lines indicate the boundaries of the cavity.**

The finding helps to explain the numerical results of Bountin et al. [7]. In their study, it was shown that the second mode is damped by the wavy surface in the frequency band from 110 to 150 kHz, while the disturbance amplitude increases for frequencies less than 110 kHz and remains almost unchanged for frequencies larger than 150 kHz. It is well-known that the location of the synchronization point is in inverse proportion to the frequency [4] so that most cavities of the wavy surface are located upstream of the synchronization point for relatively low frequencies. As a result, the second mode is amplified. Under high-frequency conditions, there are cavities located further downstream of the corresponding synchronization point, which is detrimental to the overall stabilization effect.

### C. Evolution of second mode across the cavity

As shown in Fig. 6, the second mode is strongly damped across the cavity when it is placed downstream of the synchronization point. To understand the development of the second-mode wave in the vicinity of the cavity, the instantaneous contours of pressure disturbances for cases 3 and 4 as well as the baseline flat-plate case are shown in Fig. 8. For the flat-plate case, the disturbances in the boundary layer after  $x = 0.105$  m correspond to the second mode, which propagates downstream with the phase velocity slightly lower than the velocity at the boundary-layer edge. Interpreted as trapped acoustic waves, the second-mode wave travels between the wall and the sonic line (relative to the phase velocity) and induces the two-cell structures of the pressure disturbance field. For cases 3 and 4, the basic features are similar to the flat-plate result upstream and downstream of the cavity; however, the pressure disturbance fields are strongly distorted around the cavity. Significant disturbances can be seen inside the cavity, which is in contrary to the experimental observations on the boundary-layer flows around a roughness element. The disturbances in the separation region behind the roughness element has been shown to be much smaller than those in the upper boundary layer by Tang et al. [19]. They modeled the second mode around a roughness element as sound waves passing a vortex sheet between two high-speed regions and proved that the second mode cannot penetrate the shear

layer. As a result, the second-mode wave around the wall region weakens as the majority of the acoustic wave is not present in the region according to Fong [20].

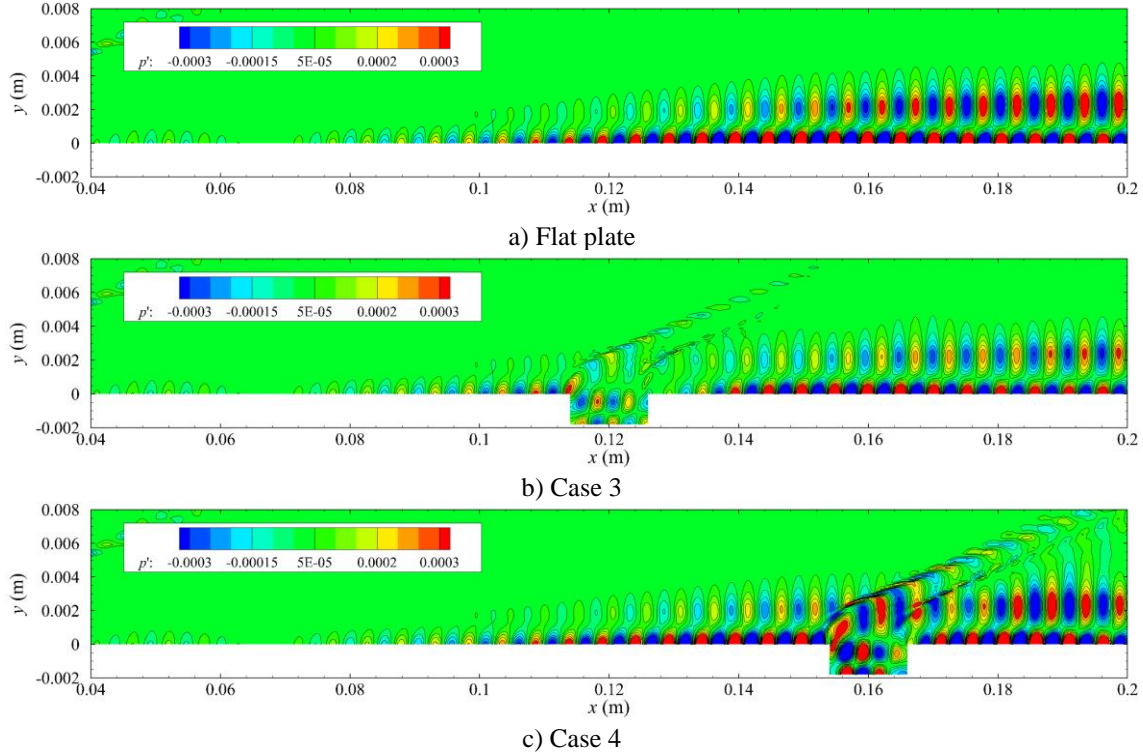


**Fig. 8 Instantaneous pressure disturbance fields for different cases.**

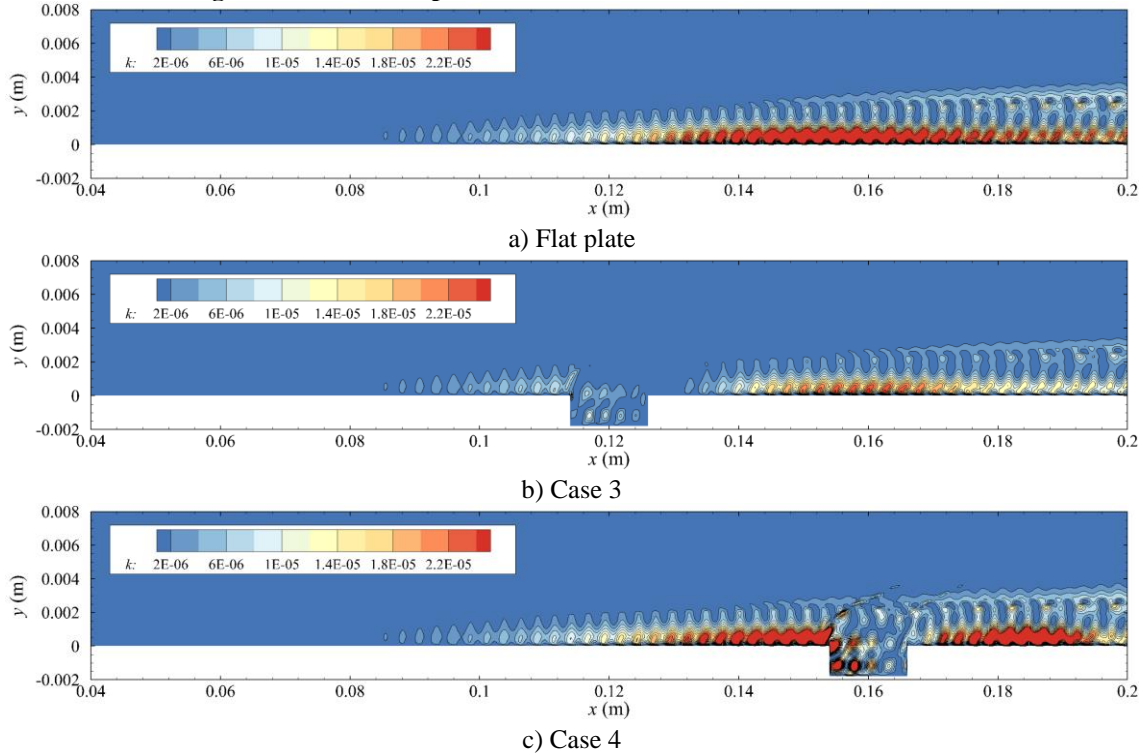


**Fig. 9 Instantaneous pressure disturbance fields for different cases.**

Although the flow structures around the cavity and roughness element are similar, the stabilization mechanisms are completely different and yet to be investigated. The pressure disturbances inside the cavity cross the zero axis twice, indicating that the instability corresponds to the third mode [21]. Similar to the finding of Balakumar et al. [8],

the second-mode disturbances become the third-mode disturbances when they propagate across the separation region, and these third-mode disturbances change back into the second mode downstream.

Figure 9 shows the contours of the instantaneous disturbance energy for different cases. Here, the disturbance energy is defined as  $k = (u'u' + v'v')/2$ . It is seen that the second-mode wave enters the cavity and experiences strong damping. Take case 4 as an example, the disturbance energy is reduced by a factor of 20 inside the cavity.

To explain the damping phenomenon, the thermoacoustic interpretation of the unstable mode recently proposed by Kuehl [22] is adopted in this study. In this theory, it has been demonstrated that the second-mode wave in hypersonic boundary layers is consistent with a thermoacoustic standing wave trapped in a thermoacoustic impedance well and derives energy from the base flow through the thermoacoustic Reynolds stress. Starting from the Navier–Stokes equations, one can easily obtain the following acoustic energy equation:

$$\frac{1}{2}\rho \frac{DV^2}{Dt} + \frac{1}{2\rho c^2} \frac{Dp^2}{Dt} = -\frac{\partial(pu_i)}{\partial x_i} + u_i \frac{\partial \tau_{ij}}{\partial x_j} + \frac{\gamma-1}{\gamma} \left( \frac{\partial q_i}{\partial x_i} + \tau_{ij} \frac{\partial u_i}{\partial x_j} \right), \quad (6)$$

where  $c$  is the speed of sound and  $V^2 = u^2 + v^2$ . It is assumed that the flow variables  $\phi$  can be decomposed into  $\phi = \bar{\phi} + \phi'$ , where  $\bar{\phi}$  denotes the mean-flow part and  $\phi'$  is the disturbance. Then Eq. (6) can be linearized into the disturbance energy equation expressed as

$$\underbrace{\frac{De'}{Dt}}_{\text{Disturbance energy}} = \underbrace{-\frac{\partial}{\partial x_i} (p'\bar{u}_i + \bar{p}u'_i + p'u'_i)}_{\text{Inviscid term}} + \underbrace{\left[ u_i \frac{\partial \tau_{ij}}{\partial x_j} + \frac{\gamma-1}{\gamma} \left( \frac{\partial q_i}{\partial x_i} + \tau_{ij} \frac{\partial u_i}{\partial x_j} \right) \right]'}_{\text{Viscous term}}. \quad (7)$$

With the cubic nonlinearity and viscous effects neglected, the so-called cycle-average disturbance energy equation can be obtained as

$$\underbrace{\frac{D\langle e' \rangle}{Dt}}_{\text{Disturbance energy}} = -\left\langle \frac{\partial}{\partial x_i} (p'u'_i) \right\rangle = -R \underbrace{\left\langle \frac{\partial}{\partial x_i} (\rho'T'\bar{u}_i + \bar{\rho}T'u'_i + \bar{T}\rho'u'_i) \right\rangle}_{\text{Thermoacoustic Reynolds stress}}, \quad (8)$$

where  $R$  is the gas constant. Time averaging is performed over the period corresponding to the actuating frequency to separate the time scales of wave oscillation and disturbance growth. Note that the second equality in this equation is derived via the equation of state. Clearly, the thermoacoustic Reynolds stress acts as an energy source so that the second mode will be amplified where it is negative.

Figure 10 shows the contour of the thermoacoustic Reynolds stress for case 4. As seen from the figure, regions of negative values occur in the boundary layer after the synchronization point corresponding to the second-mode amplification. Inside the cavity, the negative region of the thermoacoustic Reynolds stress shrinks significantly, which explains the damping of the disturbances.

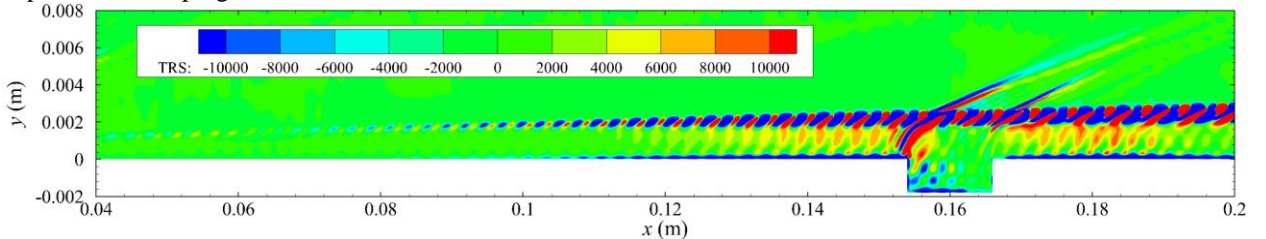


**Fig. 10 Thermoacoustic Reynolds stress contour for case 4.**

## V. Conclusions

In this study, the stabilization of a hypersonic boundary layer with a local two-dimensional cavity is investigated using direct numerical simulations. Four cases are considered with the cavity located upstream or downstream of the synchronization point of mode F and mode S. The results indicate that cavity location plays an important role in the development of mode S excited by wall blowing-suction. When the cavity is placed upstream or further downstream

of the synchronization point, the second mode is destabilized. In contrast, the second mode is stabilized only if the cavity is placed closely downstream of the synchronization point. The stabilization effect of the relative location between the cavity and the synchronization point is similar to those for a local roughness element and a heating trip. The disturbances are significantly damped inside the cavity located downstream of the synchronization point, which can be explained by the thermoacoustic interpretation. It is suggested that an efficient way to stabilize the boundary layer is to put a local cavity in the close downstream region of the synchronization point corresponding to the most dangerous frequency.

### Acknowledgments

The authors would like to thank the Hong Kong Research Grants Council (no. 152151/16E) the National Natural Science Foundation of China (no. 11772284) for financial support. The authors are also grateful to the National Supercomputer Center in Tianjin for providing computational resource.

### References

- [1] Zhong, X. and Wang, X., "Direct Numerical Simulation on the Receptivity, Instability, and Transition of Hypersonic Boundary Layers," *Annual Review of Fluid Mechanics*, Vol. 44, 2012, pp. 527–561.
- [2] Fedorov, A. and Tumin, A., "Transition and Stability of High-Speed Boundary Layers," *Annual Review of Fluid Mechanics*, Vol. 43, 2011, pp. 79–95.
- [3] Zhao, R., Wen, C. Y., Tian, X. D., Long, T. H., and Yuan, W., "Numerical Simulation of Local Wall Heating and Cooling Effect on the Stability of a Hypersonic Boundary Layer," *International Journal of Heat and Mass Transfer*, Vol. 121, 2018, pp. 986–998.
- [4] Duan, L., Wang, X., and Zhong, X., "Stabilization of a Mach 5.92 Boundary Layer by Two-Dimensional Finite-Height Roughness," *AIAA Journal*, Vol. 51, No. 1, 2013, pp. 266–270.
- [5] Fong, K. D., Wang, X., Huang, Y., Zhong, X., McKiernan, G. R., Fisher, R. A., and Schneider, S. P., "Second Mode Suppression in Hypersonic Boundary Layer by Roughness: Design and Experiments," *AIAA Journal*, Vol. 53, No. 10, 2015, pp. 3138–3143.
- [6] Wang, X. and Zhong, X., "The Stabilization of a Hypersonic Boundary Layer Using Local Sections of Porous Coating," *Physics of Fluids*, Vol. 24, 2012, 034105.
- [7] Bountin, D., Chimitov, T., Maslov, A., Novikov, A., Egorov, I., Fedorov, A., and Utyuzhnikov, S., "Stabilization of a Hypersonic Boundary Layer Using a Wavy Surface," *AIAA Journal*, Vol. 51, No. 5, 2013, pp. 1203–1210.
- [8] Balakumar, P., Zhao, H., and Atkins, H., "Stability of Hypersonic Boundary Layers over a Compression Corner," *AIAA Journal*, Vol. 43, No. 4, 2005, pp. 760–767.
- [9] Hao, J., Wang, J., and Lee, C., "Numerical Study of Hypersonic Flows over Reentry Configurations with Different Chemical Nonequilibrium Models," *Acta Astronautica*, Vol. 126, 2016, pp. 1–10.
- [10] Hao, J., Wang, J., and Lee, C., "Development of a Navier–Stokes Code for Hypersonic Nonequilibrium Simulations," *21st AIAA International Space Planes and Hypersonics Technologies Conference*, AIAA Paper 2017-2164, 2017.
- [11] Hao, J., Wang, J., and Lee, C., "Numerical Simulation of High-Enthalpy Double-Cone Flows," *AIAA Journal*, Vol. 55, No. 7, 2017, pp. 2471–2475.
- [12] Hao, J. and Wen, C. Y., "Numerical Investigation of Oxygen Thermochemical Nonequilibrium on High-Enthalpy Double-Cone Flows," *International Journal of Heat and Mass Transfer*, Vol. 127, 2018, pp. 892–902.
- [13] Hao, J., Wang, J., and Lee, C., "Numerical Simulation of High-Enthalpy Hollow-Cylinder/Flare Flows," *AIAA Journal*, Vol. 56, No. 8, 2018, pp. 3337–3341.
- [14] McCormack, R. W., *Numerical Computation of Compressible and Viscous Flow*, AIAA Education Series, AIAA, Reston, VA, 2014, pp. 181–185.
- [15] Van Leer, B., "Towards the Ultimate Conservative Difference Scheme," *Journal of Computational Physics*, Vol. 32, No. 1, 1979, pp. 101–136.
- [16] Wright, M. J., Candler, G. V., and Bose, D., "Data-Parallel Line Relaxation Method for the Navier–Stokes Equations," *AIAA Journal*, Vol. 36, No. 9, 1998, pp. 1603–1609.
- [17] Wang, X., Zhong, X., and Ma, Y., "Response of a Hypersonic Boundary Layer to Wall Blowing-Suction," *AIAA Journal*, Vol. 49, No. 7, 2011, pp. 1336–1353.
- [18] Fedorov, A. and Tumin, A., "High-Speed Boundary-Layer Instability: Old Terminology and a New Framework," *AIAA Journal*, Vol. 49, No. 8, 2011, pp. 1647–1657.
- [19] Tang, Q., Zhu, Y., Chen, X., and Lee, C., "Development of Second-Mode Instability in a Mach 6 Flat Plate Boundary Layer with Two-Dimensional Roughness," *Physics of Fluids*, Vol. 28, 2015, 064105.
- [20] Fong, K. D., "A Numerical Study of 2-D Surface Roughness Effects on the Growth of Wave Modes in Hypersonic Boundary Layers," Ph.D. Dissertation, Univ. of California Los Angeles, Los Angeles, CA, 2017.
- [21] Mortensen, C. H., "Toward an Understanding of Supersonic Modes in Boundary-Layer Transition for Hypersonic Flow over Blunt Cones," *Journal of Fluid Mechanics*, Vol. 846, 2018, pp. 789–814.
- [22] Kuehl, J. J., "Thermoacoustic Interpretation of Second-Mode Instability," *AIAA Journal*, Vol. 56, No. 9, 2018, pp. 3585–3592.